Control Device Effectiveness Studies of a 53° Swept Flying Wing Configuration. Experimental, Computational, and Modeling Considerations.

Patrick Löchert[a,1], Kerstin C. Huber[b], Mehdi Ghoreyshi[c], Jacob Allen[c]

[a]German Aerospace Center (DLR), Braunschweig, Germany
[b]German-Dutch Wind Tunnels (DNW), Göttingen, Germany
[c]High Performance Computing Research Center, U.S. Air Force Academy, CO 80840, USA

Abstract

The present investigation covers studies of different control devices on several 53° swept flying wing configurations without a vertical tail plane. The wings considered share the same planform but differ in their spanwise profile shapes. The planform, developed under the NATO AVT-251 Task Group, is referred to as the MULDICON (or MULti-DIsciplinary CONfiguration). The objectives of this article are twofold: (1) to design yaw control surfaces for the MULDICON wing using an experimental/computational approach and (2) to develop aerodynamic models that rapidly and accurately predict the effectiveness of control surfaces over a wide range of flight conditions. The yaw control surface design (position and size) should provide sufficient yaw moment with almost no contribution in roll and pitch moment. To identify such concepts, a number of preliminary experiments on a generic flying wing configuration have been conducted. Two promising concepts from wind tunnel tests were then numerically examined for being implemented in the MULDICON baseline wing. Concepts with spoilers and a split flap were specifically considered. For medium to high angles of attack, the flow topology of the baseline wing is dominated by a vortical flow field on the upper outer wing. This leads to interactions between vortex and the control device which influences the flow and the attitude of the control device on the upper wing side. Furthermore, this work considers developing aerodynamic models for predicting stability derivatives of several MULDICON designs over a wide range of flight conditions. Aerodynamic loads models are only developed for normal force and pitch moment coefficients, however, the developed approach can easily being extended to include lateral aerodynamic coefficients as well. Quasi-steady models of this work are power series expansions of traditional linear aerodynamic models to capture nonlinear effects. Additionally, the models can estimate static and dynamic stability derivatives and the control surface powers.

Keywords:
CFD, highly swept wing, stability and control, tailless flying wing, vortex dominated flow, system identification, training maneuver

Nomenclature

a	acoustic speed, $\mathrm{m\,s^{-1}}$
c	reference chord length, m
C_D	drag coefficient, $D/q_\infty \cdot S$
C_l	rolling moment coefficient
ΔC_l	Difference in C_l between configuration with and without control devices
C_m	pitching moment coefficient
ΔC_m	Difference in C_m between configuration with and without control devices
$C_{m\alpha}$	pitching moment curve slope, 1/rad
C_{mq}	pitching moment due to q, 1/rad
$C_{m\dot{\alpha}}$	pitching moment due to $\dot{\alpha}$, 1/rad
C_n	yawing moment coefficient
ΔC_n	Difference in C_n between configuration with and without control devices
C_N	normal force coefficient
$C_{N\alpha}$	normal force curve slope
C_{Nq}	normal force due to q
$C_{N\dot{\alpha}}$	normal force due to $\dot{\alpha}$
k	reduced frequency, $\frac{\omega \cdot c}{2V_\infty}$
M_∞	Mach number
q	normalized pitch rate
t	time, s
Re_∞	Reynolds number, $\frac{V_\infty \cdot l}{\nu}$
t^*	normalized time step, $\frac{t \cdot V_\infty}{c}$
V_∞	free-stream velocity, m/s
ASG	Aerodynamic Shaping Group
AVT	Applied Vehicle Technology
CCG	Control Concept Group
CFD	Computational Fluid Dynamics
DLR	German Aerospace Center
DNW	German-Dutch Wind Tunnels
IB	inboard flap
LE	leading edge
MPM	Model Positioning Mechanism
MULDICON	Multi-Disciplinary Configuration
OB	outboard flap
RANS	Reynolds averaged Navier Stokes
SA	Spallart-Allmaras
SACCON	Stability and Control Configuration

Email addresses: `patrick.loechert@dlr.de` (Patrick Löchert), `kerstin.huber@dnw.aero` (Kerstin C. Huber), `mehdi.ghoreyshi@usafa.edu` (Mehdi Ghoreyshi), `jallen12000@gmail.com` (Jacob Allen)

[1]Corresponding Author.

SID	System identification
STO	Science and Technology Organization
TE	trailing edge
USAFA	United States Air Force Academy

Greek

α	angle of attack, rad
$\dot{\alpha}$	normalized time rate of change of α
β	angle of sideslip, rad
μ	air viscosity, $\mathrm{kg\,s^{-1}m^{-1}}$
ρ	air density, $\mathrm{kg\,m^{-3}}$
ν	kinematic viscosity
φ	sweep angle, degree
δ	control surface deflection angle, degree
θ	pitch angle, deg
ω	angular frequency, rad/s

1. Introduction

The design constraints of future agile and low observable Unmanned Combat Air Vehicle (UCAV) configurations are a compromise between a minimum cross section and an advanced flight performance to achieve long range with remaining agility. As a result, the current trend in the UCAV design is toward using medium to highly swept wings with round or variable leading edge (LE) geometries. Specifically, the performance and signature considerations often result in medium leading edge sweep angles in range of $45° - 60°$.

The objectives of this study are related to the NATO STO AVT-251 Task Group [1], which was established to computationally design a new Multi-Disciplinary configuration, named MULDICON from previous NATO Task Group experiences to meet a set of desired mission requirements. The design of MULDICON needs to achieve satisfactory performance and handling characteristics and therefore should engage all participants in a collaborative effort. To facilitate these needs, different subgroups were established including: Design specification and Assessment Group (DSAG), Aerodynamic Shaping Group (ASG), Engine Integration Group (EIG), Control Concept Group (CCG), and Structural Concept Group (SCG). This article summarizes two different studies that were conducted independently within ASG and CCG.

A number of designs were evaluated; all these designs share a similar planform but they have different cross-sections. Designs considered in this work are the baseline planform and the ASG Design2 wing. The baseline wing is similar to the AVT-161 configuration (named SACCON) but exhibits a TE sweep angle of $\varphi_{TE} = 30°$, whereas the airfoils remain like the ones of the SACCON. This wing was used in the studies of the control concept group and therefore is called here CCG wing for convenience. The ASG Design2 wing was created within the Aerodynamic Shaping Group. The objective of this group was to computationally design a flyable vehicle based on the baseline planform to meet a desired mission. For example, the design should have a lift coefficient of 1.0 during takeoff and landing ($M_\infty = 0.2$) and reach $C_L = 0.5$ at high altitude and high Mach

number ($M_\infty = 0.8$). These requirements cannot be met by the AVT-161 SACCON configuration or the baseline design. The aerodynamic performances of baseline and the ASG Design2 wings were detailed and compared in Ref. [2]. The study concluded that the Design2 wing indicates an improvement in sustained turn performance and is a considerable improvement over the baseline wing.

A challenge in the design of MULDICON is to achieve high agility and flight performance without a vertical tail plane for yaw control to reduce the radar cross section [3]. These types of configurations have a strong nonlinear aerodynamic behavior due to the flow dominated by complex vortex systems, including vortex-to-vortex and vortex-to-boundary layer interactions. For these reasons, investigations on the influence and effectiveness of alternative control concepts for yaw controllability are necessary. Due to the vortical flow field on the upper wing side of SACCON for medium to high angles of attack (AoA), a control-device/vortex interaction occurs. In a previous study by Winkler et al. [4], the influence of the vortex dominated flow field on the effectiveness of unconventional spoiler geometries at the trailing edge (TE) was demonstrated.

The present investigation analyses the effects of the aerodynamic behavior of different alternative yaw control devices on the CCG wing. The boundary conditions of the required effectiveness of the control device result from the flight mechanical requirements acquired in the NATO STO AVT-251 research Task Group by Liersch et al. [5]. The summarized flight mechanical requirement for the presented studies is a necessary yawing moment C_n of at least $1.5 \cdot 10^{-2}$ with an almost neutral influence on roll and pitch moments. In order to keep the radar cross section low, the deflection and the size of the control surfaces is restricted and should be as small as possible. Regarding the necessary yawing moment, a maximized lever arm for this type of control surface is favorable. For this reason, flap based control concepts like spoiler and split flaps have been applied and assessed within a design study of the control concept group.

The second challenge in the MULDICON design and stability and control study was related to the computational cost of generating CFD datasets for the control device effectiveness study which might require several hundreds of simulations (combinations of angle of attack, Mach number, and control device deflections). Many efforts on reducing the computational cost and accelerating the generation of such a dataset have been demonstrated, for example see Refs. [6, 7, 8]. Specifically, Allen and Ghoreyshi [8] presented several prescribed maneuvers and aerodynamic models that accurately and rapidly predict the aerodynamic stability derivatives of a generic missile configuration over a wide range of air speeds using CFD simulations. This work follows-up the work of Allen and Ghoreyshi [8] to develop aerodynamic models for different MULDICON planforms (CCG and ASG wings) with moving control surfaces. Aerodynamic loads models are only developed for normal force and pitch moment coefficients, however, the developed approach can easily be extended to include lateral aerodynamic coefficients as well. This article is organized as follows: first, test cases are described. Experimental efforts on the development of spoiler yaw control surfaces are then summarized. This is followed by a description of numerical approaches including the used flow solvers, computational setups, system identification modeling approach, and generation of training maneuvers. Results will present the computational predictions of spoiler and split flaps for the yaw control, the validation of aerodynamic models, and their prediction capabilities. Finally, the conclusions will be drawn.

2. Test Cases

The MULDICON planform and its geometrical dimensions are shown in Figure 1.

A more detailed description of the configuration can be found in Cummings et al. [1]. For a better comparison between the moment coefficients, all moment coefficients are normalized with the same reference length of $c_{ref} = 6m$. CCG and ASG wing designs are considered in this article, both used for the aerodynamic modeling study. The CCG wing has airfoil sections similar to the ones used in the SACCON wing. The SACCON was designed in a preceding NATO STO-AVT-161 Task Group to investigate the Stability and Control behavior of a highly swept flying wing configuration and is described in Cummings and Schütte et al. [9]. The ASG wing has a similar planform to the CCG wing but different airfoil cross-sections. The design philosophy used in the ASG wing was

Figure 1: MULDICON geometry.

to have attached flow on the wing across all design points by delaying the onset of flow separation beyond those required for operation. The design approach used a linear theory that relied on combining a series of chordwise and spanwise deflection modes to yield design camber and twist, minimizing drag for a given Mach number and C_L combination with or without a C_m constraint. Then by iteration and analysis of low speed and high speed properties, a "good" compromise design was achieved. Figure 2 compares the airfoil sections of CCG and ASG wings.
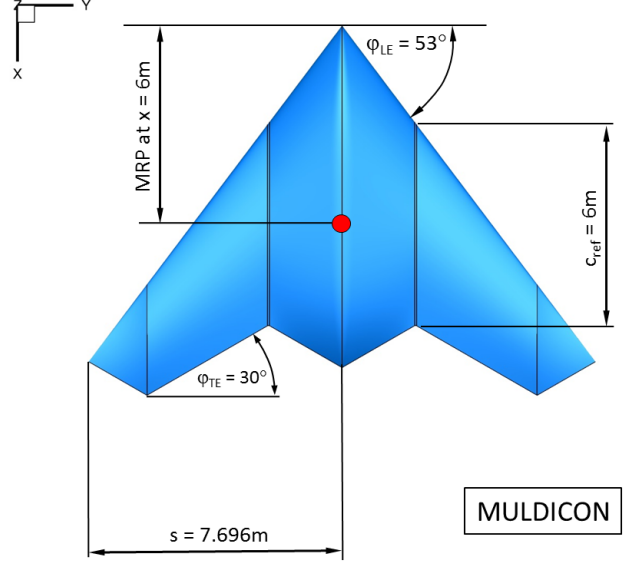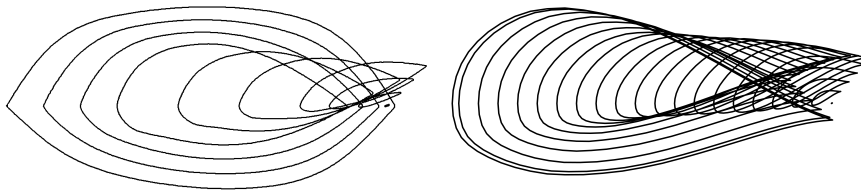

Figure 2: Airfoil sections for CCG (left) and ASG (right) wings.

The CCG wing was used for the control device study with an approach flight speed of $M_\infty = 0.4$ at sea level and a Reynolds number of $Re_\infty = 55.9 \cdot 10^6$. Due to the similar planform, leading edge sweep angle, and radius contour of the CCG wing and SACCON configuration, the flow topology of both configurations are comparable for the same onflow conditions. The SACCON's flow topology was described in Zimper and Hummel [10]. The resulting flow topology of the CCG wing for the here considered flight condition is presented in Figure 3. It shows the pressure coefficient and the skin friction lines for the CCG wing at angles of 8° and 12° from numerical

investigations with a RANS method of the DLR TAU flow solver. At $\alpha = 8°$, a separation at the sharp leading edge apex has developed which becomes larger with increasing AoA. Integrating a yaw control device at the wingtip will become affected by the tip vortex, which occurs at $\alpha \approx 8°$ and its onset point moves towards the apex along the LE with increasing AoA.
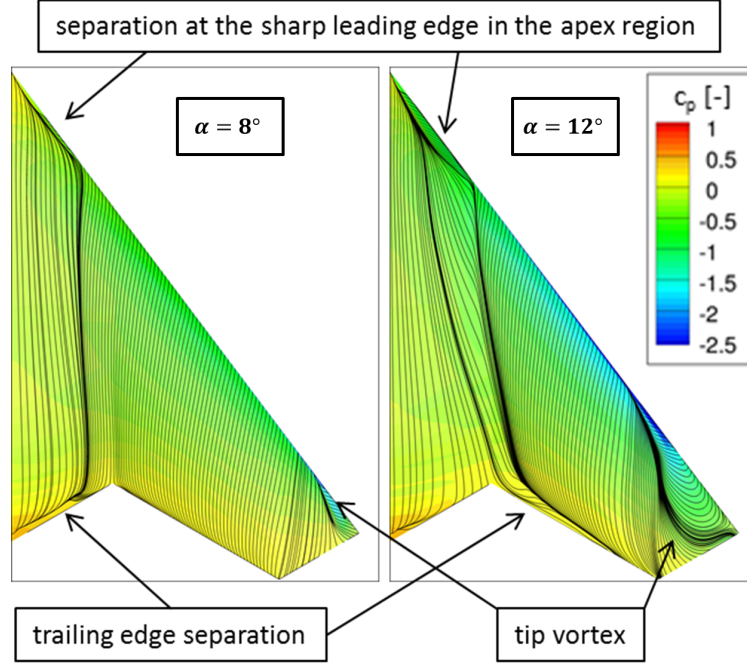

Figure 3: The CCG wing flow topology ($M_\infty = 0.4$, $Re_\infty = 55.9 \times 10^6$).

3. Experimental Approach

Preceding experimental investigations conducted within the low-speed regime with the DLR-F19 wind tunnel model lead to the development of the spoiler concept of the MULDICON. A summary of results are presented in this section. The DLR-F19 is based on the SACCON and accommodates control devices as described in Cummings and Schütte [9]. The wind tunnel model was designed at the DLR Institute of Aerodynamics and Flow Technology, structurally dimensioned by Leichtwerk AG and was built at the DLR Braunschweig workshop. The DLR-F19 model is dimensioned for static as well as dynamic testing, up to a maximum velocity of $V_\infty = 90\frac{m}{s}$ ($M_\infty = 0.256$). The model has a weight of approximately 10 kg and can be equipped with a wide range of different control surfaces along the TE as well as with spoiler geometries within the body region of the configurations upper side. The model dimensions of the DLR-F19 as well the test set up in the wind tunnel with the Model Position Mechanism (MPM) model support in the DNW-NWB are given in Figure 4.

The model has been subjected to a number of experimental test campaigns. Through the first three low speed wind tunnel experiments, the effects of conventional trailing edge control surfaces have been studied [11]. The model has then been equipped with non-conventional control surfaces, namely spoilers. The tests have been conducted at the low speed DNW-NWB Braunschweig at a Mach number of $M_\infty = 0.15$.
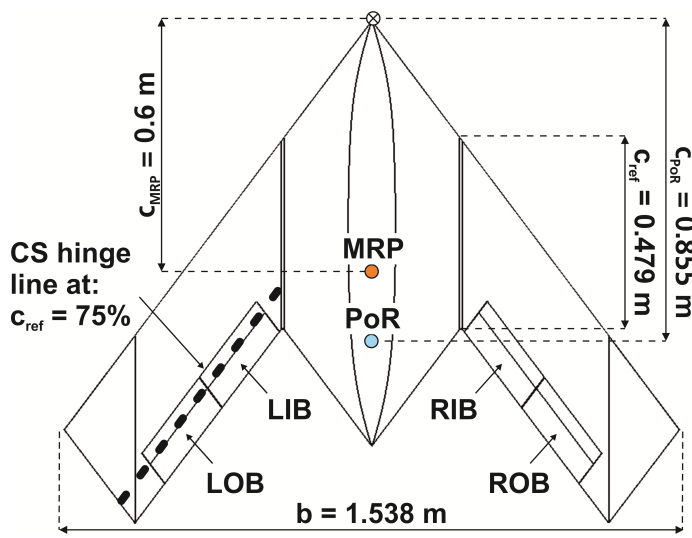
(a) Dimensional Layout DLR-F19

(b) DLR-F19 on belly sting

Figure 4: Experimental setup on the MPM of the DNW-NWB using DLR-F19 configuration.
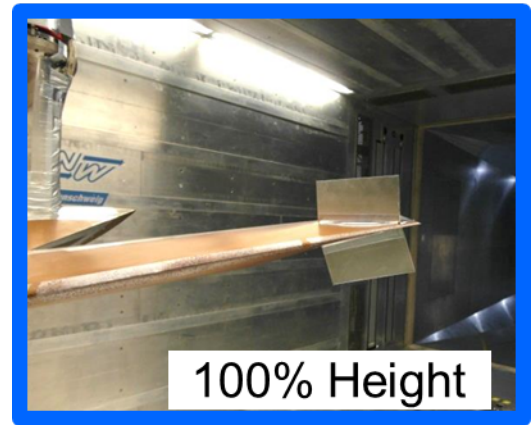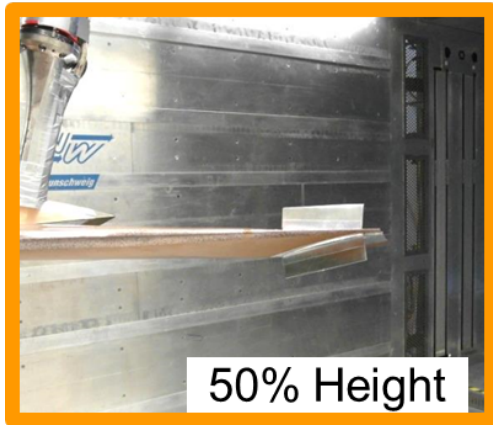

Figure 5: Experimental setup with a double sided spoiler on the wingtip of DLR-F19 configuration.

Throughout the test campaign, all tested configurations, apart from one, gave rise to coupled influence on all moment coefficients. This means that no isolated influence of the yawing moment coefficient from the others could be achieved. One configuration, however, was identified where only the yawing moment was influenced by the spoiler but not the pitching and rolling moment. For this particular setup, the spoiler is located on the upper and lower side at the wingtip, deflected perpendicular to the flow with a deflection angle of $\delta_u = 90°$ at the upper and $\delta_l = 90°$ on lower side. The experimental setup for this particular spoiler configuration for two different spoiler heights can be seen in Figure 5.

As it can be seen from Figure 6, the spoiler setups give rise to a coupled set of coefficients for AoA $\alpha > 8°$. When however the height of the spoiler is reduced a sole influence in yaw, though also reduced in value, can be achieved up to an AoA of $\alpha = 10°$. Furthermore the control device

7

(a) Yawing moment distribution
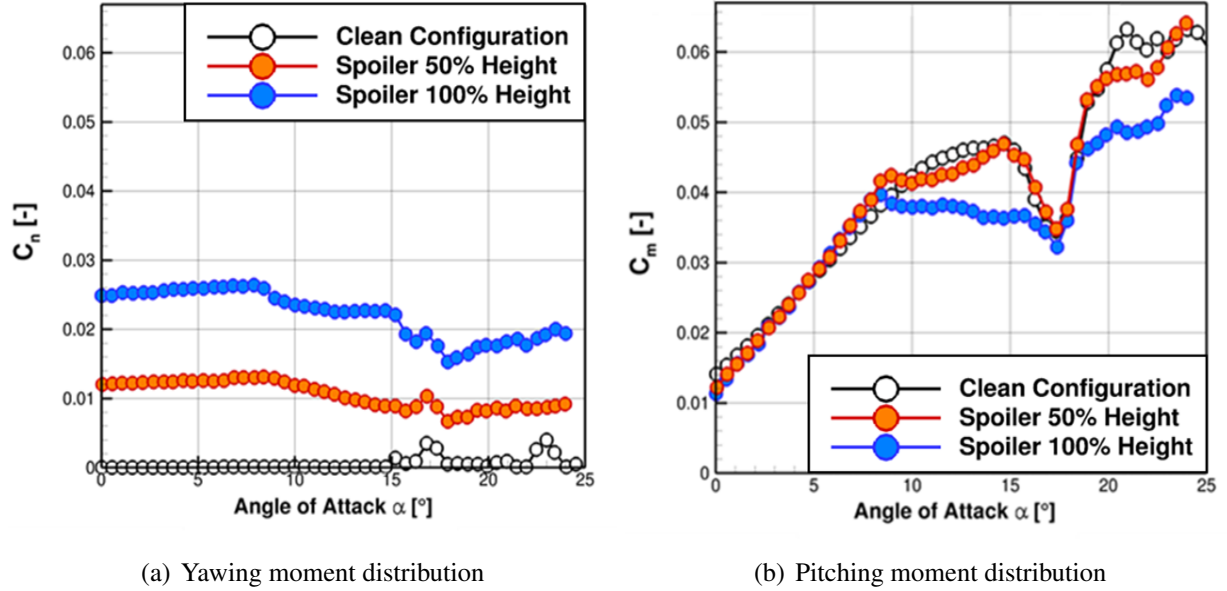(b) Pitching moment distribution

Figure 6: Influence on the pitching and yawing moment by experimental results with spoiler located within the wingtip region on the DLR-F19 configuration.

offers a nearly constant yawing moment over the AoA up to $\alpha = 10°$. For higher AoA the yawing moment efficiency decreases and the differences of the pitching moment increases. So a feasible controllability with this configuration at higher AoA is not given. The spoiler setup used in this experimental investigation was chosen for a first control concept for the numerical investigations of the MULDICON, which will be discussed in section 5.1.1.

4. Numerical Approach

4.1. CFD Solvers

4.1.1. TAU

The DLR flow solver TAU is used for simulation of yaw control devices on the CCG wing. The code solves the compressible three-dimensional RANS equations and is being developed by the DLR Institute of Aerodynamics and Flow Technology [12]. The solver is based on a finite volume formulation. For simulations of this work, a cell vertex metric is used in combination with a multigrid approach. DLR TAU can be applied on unstructured hybrid grids which allow working with different types of elements. Prismatic elements are used to resolve the viscous shear layers close to the walls, whereas the remaining field is resolved with tetrahedral elements. For the presented simulations, the one-equation Spalart-Allmaras (SA) turbulence model in its negative form (SA-neg) is used. The SA-neg formulation is less sensitive to particularly negative values of the transport turbulence quantities [13].

4.1.2. Kestrel

The *Kestrel* CFD solver, KCFD, was used for the aerodynamic modeling study. *Kestrel* was developed under the DoD High Performance Computing Modernization Program's (HPCMP) Computational Research and Engineering Acquisition Tools and Environments (CREATE^{TM}) program. *Kestrel* is part of the CREATE Air Vehicles (CREATE-AV) software initiative. The purpose of the CREATE program is to develop multi-disciplinary physics-based computational engineering tools that will increase the efficiency of the acquisition process. The *Kestrel* software specializes in fixed wing, full vehicle aerodynamic analysis.

Kestrel was developed with a modular architecture, such that new capabilities can be added to the code as they are developed with relative ease. This allows the user to expose and use capabilities as needed, thereby making the software applicable to many areas of aircraft aerodynamic analysis. The KCFD solver, used in this work, is a finite-volume cell-centered solver which can run with mixed element type unstructured meshes. The Method of Lines is used to separate the temporal and spatial integration. This allows a second-order accurate Godunov scheme to be employed in space, as well as a second-order subiterative point-implicit scheme in time.

Arbitrary prescribed body maneuvers (which are rigid-body transformations of the mesh relative to the reference flow) can be specified in *Kestrel* through a user-generated text file. *Kestrel* accepts three formats for this file. For this work, the "Euler Angle" file type was used. The motion file is formatted by listing the Euler angles and any mesh translations at discrete and increasing times. For this work, new angles and translations are specified at the simulation time step. Using this format for motion specification allows for the aircraft pitch, and subsequently q, to be explicitly specified, while allowing for an independent angle of attack to be achieved by mesh translations relative to the reference flow.

A body hierarchy is used in *Kestrel*, which lets the user define parent and child bodies. This hierarchical structure applies any transformations of the parent body automatically to the child bodies. In addition, any forces acting on the child bodies are automatically added to the parent body. Overset control surfaces can be added as a special type of child body to the parent aircraft. Arbitrary control surface deflections can be specified using another motion file, similar to the arbitrary prescribed body motion. The arbitrary control surface motion file allows the hinge line and the angle of deflection to be specified at discrete and increasing times. Details about the *Kestrel* software can be found in the *Kestrel* user's guide [14].

4.2. Computational Setups

The hybrid unstructured grids used for the yaw control surface simulations have been generated with the hybrid grid generator Centaur, developed by CentaurSoft [15]. For all hybrid grids, the initial layer thickness of the first prismatic layer is 0.005mm, resulting in a typical y+ value of approximately one. The boundary layer is fully resolved using 30 prismatic layers. Over the entire surface of the configuration, the full 30 prismatic layers can be achieved, hence no chopping of prismatic layers occurs. The hybrid unstructured grid can be seen in Figure 7 with the tetrahedral field grid in green on the left and an enlarged view for surface triangulation in turquoise and the prismatic layers in red on the right. For the integration of the yaw control device at the wingtip, a modular grid approach was used. Hereby the grid around the configuration is divided into a main grid and a sub-grid. The main grid remains the same for all simulations and only a part of the

(a) Tetrahedral field grid   (b) Prismatic layer and surface resolution around CCG wing.
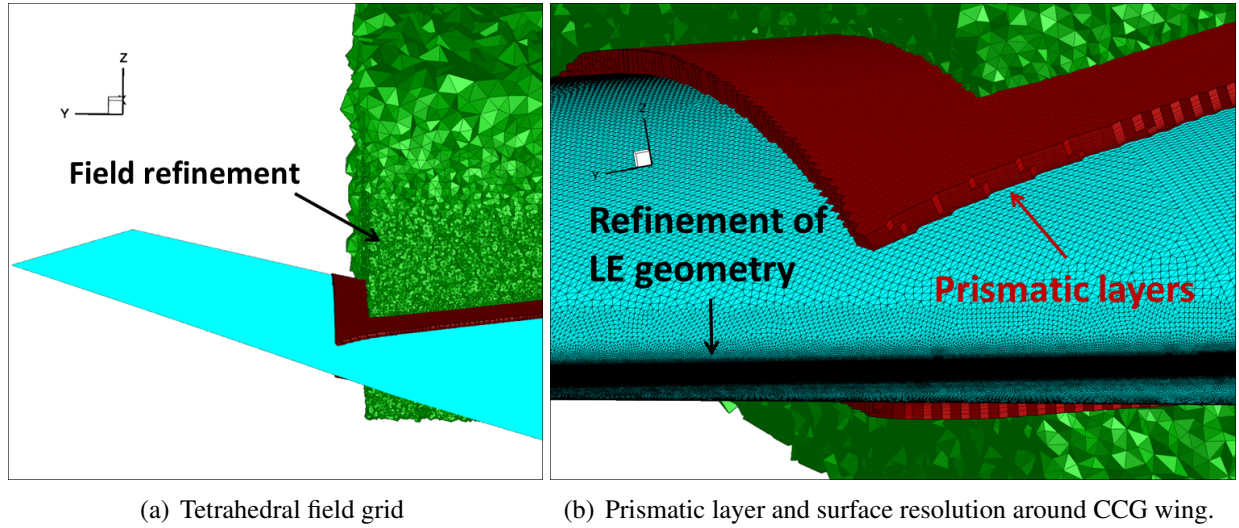
Figure 7: Numerical grid

geometry within a predefined bounding box (module) is being remeshed (sub-grid). Using this approach the time for the mesh generation can be significantly decreased. In the here presented case, the module is placed around the wingtip and its panels are defined as interface panels to the main grid, hence any control device configuration located within the module at the wingtip can be meshed. First the main grid is generated, and after the main grid generation, the geometry within the module can be exchanged and only the grid within the module is being newly generated. The nodes on every interface panel from the main grid to the module are fixed and are used for the modular grid generation. This guarantees a continuous connection of both, the main grid and the sub-grid. This approach also allows for resolution of the LE which remains constant with spoiler geometry change; by this means the leading edge always triggers the same vortical flow field along the LE. With this strong similarity between all used grids a high comparability between the different grids can be achieved, with similar spatial discretization errors. The overall grid sizes amount to approximately 61 million nodes for a full model setup. The present numerical approach is validated for the SACCON with control devices and documented by Liersch et al. [16] and Schütte et al. [17].

The grids used for the system identification of CCG and ASG wings are shown in Figure 8. These wings have two conventional flaps on each side of the wing; the flaps are similar to those used for DLR-F19 configuration shown in Figure 4. The grids for the half-body geometries were made using Pointwise version 18. In addition, grids for the inboard and outboard flaps were generated and overset to the UCAV background grid. The surface meshes of all these grids are hybrid meshes consisting mostly of patches of structured meshes connected by triangular meshes in places where structured meshes would contain too distorted cells. The main motivation for using the quadrilateral mesh is having a good grid resolution on the leading and trailing edges of the wing. The volume mesh is fully unstructured with 50 prism layers on the UCAV surface. The growing ratio of the prism layers is 1.25 and their growth is terminated when the transition between the prism layer and the tetrahedral mesh is smooth. The half-body girds have around 23.9 million nodes and 35.4 million cells. The averaged first cell grid spacing (y+) is 0.1 at $M_\infty = 0.2$.
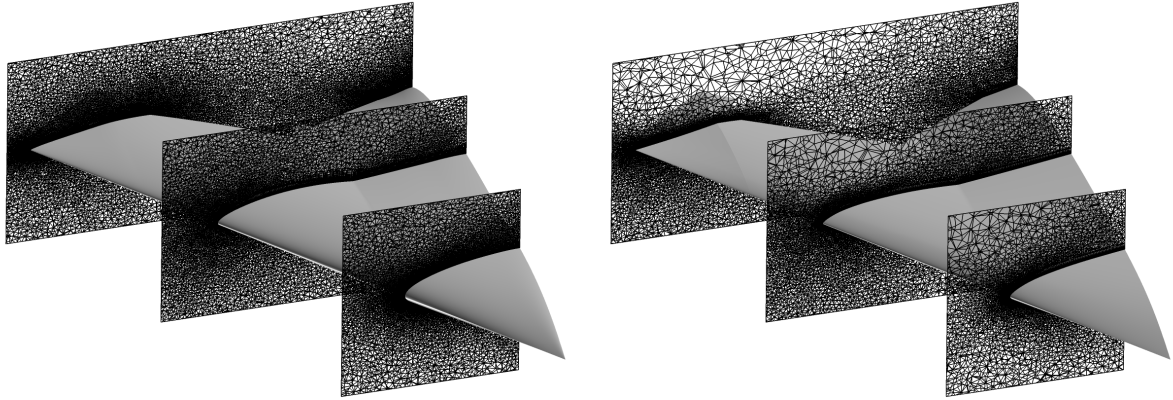
10

Figure 8: X-plane cuts of the meshes used for CCG (left) and ASG (right) wings.

Many static CFD cases are completed in *Kestrel* to create a set of validation data to compare to the system identification modeling. Static cases are completed at zero angle of attack for three Mach numbers, 0.2, 0.4, 0.8. At $M_\infty = 0.4$, three additional angles of attack are studied: 5, 10, and 15 degrees. At each of these conditions, five control surface deflections are studied: non-deflected, inboard ±20 and outboard ±20. Also at $M_\infty = 0.4$, inboard and outboard deflections of ±10 degrees are added. Finally, at $M_\infty = 0.2$ and $M_\infty = 0.8$, simulations of 5 degrees angle of attack of are completed with no control surface deflections.

All static CFD cases are run for 3,500 time steps, with data averaged over the final 1,500 time steps. A non-dimensional time step of $t^* = 0.01$ is used for all static simulations in this work. 600 start-up iterations are used to initially converge the flow. Temporal damping of 0.005, and three subiterations are used as well. For the system identification training maneuvers and other simulations including a moving grid, non-dimensional time step still remains $t^* = 0.01$ but temporal damping was set to 0.15, and subiterations increased to five which helps increasing temporal accuracy for moving mesh simulations. The system identification maneuvers are 40 seconds in length, thus requiring 22,9172 time steps. All CFD cases for the system identification used the SARC+DDES turbulence model, with which Nelson *et al.* [18] showed good accuracy for the similar SACCON configuration in *Kestrel*.

4.3. Aircraft System Identification

Determining the functional dependencies between the inputs and outputs of the aircraft system is called aircraft system identification (SID). Once these functional dependencies are established, other analyses can be completed, including stability and control analyses. System identification is a wide field in terms of the methods used to determine and model the functional relationships. Time dependent, quasi-steady, and frequency domain methods are all used to perform aircraft SID. This work uses a quasi-steady method, also referred to as a derivative-based method, where functional relationship are developed as linear polynomial equations in terms of the aircraft flight parameters and rates. No direct dependence on time is retained.

A quasi-steady model is limited in its applicability where the aircraft might experience fully unsteady flight characteristics, like dynamic stall or flutter. A useful measure for characterizing

11

the unsteadiness of fluid flow is the reduced frequency, $k = \omega c/2V_\infty$, where ω is the oscillation frequency, c is the characteristic length, and V_∞ is the freestream velocity. Generally, reduced frequencies below $k = 0.01$ are considered quasi-steady, and while results from Greenwell [19] demonstrate this, his results also demonstrate that dynamic derivatives can show large variations with reduced frequency. This demonstrates that the quasi-steady model will begin to become inaccurate as unsteady flow effects begin to dominate the aerodynamics.

The quasi-steady SID modeling in this work follows a specific process. First a training maneuver (a computational "test-flight") is completed in CFD. The training maneuver will vary any flight parameters of interest, often simultaneously, to generate training data. Once the maneuver is complete, models can be constructed using any desired technique by comparing the variations of the inputs with the calculated integrated loads (the aerodynamic coefficients). In this work, a dynamic training maneuver is completed because the effects of q and $\dot{\alpha}$ are of interest. The longitudinal integrated loads on the aircraft are studied in this work: normal force coefficient, C_N, and pitch moment coefficient, C_m. Once the models are constructed, they are used to simulate an "off-design" maneuver. The off-design maneuver is not used to train the models, but acts as a comparative data set. The training and off-design maneuvers should be different to show that the generated models are extensible to different types of maneuvers.

While parameter selection techniques can be applied to the model selection process, such as the multivariate orthogonal functions demonstrated by Klein and Morelli [20], none were applied in this work. The reason is that control over the specific terms which are included in the model must be maintained. Since the models cover the control surface influence over the Mach and angle of attack range of interest, in addition to static and dynamic stability derivatives, very specific terms are needed to ensure that estimates could be extracted for all these desired parameters. The resulting models are validated against steady CFD simulations, as well as against dynamic CFD simulations predicting dynamic stability terms and "off-design" CFD maneuvers.

Quasi-steady, derivative based SID models are used in this work. These models start from a traditional linear aerodynamic model, shown here for C_N:

$$C_N = C_{N_0} + C_{N\alpha}\Delta\alpha + C_{N\dot{\alpha}}\dot{\alpha} + C_{Nq}q + C_{N\delta_i}\Delta\delta_i \tag{1}$$

Next, the tradition model stability terms can be extended by multivariate power series to capture changes of these terms over the Mach and angle of attack range of interest, demonstrated for $C_{N\alpha}$:

$$C_{N\alpha}(M_\infty, \alpha) = \beta_0 + \beta_1(M_\infty + \alpha) + \beta_2(M_\infty + \alpha)^2 + \cdots + \beta_n(M_\infty + \alpha)^n \tag{2}$$

Every term from Eq. 1 can be expanded similarly to capture behaviors over any variables of interest. Any terms that show up twice can be combined to have a common β fit coefficient. The order of the power series expansion can be arbitrarily selected to capture expected curvatures of each stability coefficient. However, a higher order of expansion will yield more terms, increasing the opportunity for over-fitting. The final models should be compared against off-design maneuvers to ensure that they are not over-fit.

For this work, a first-order expansion for $C_{N\dot{\alpha}}$, C_{Nq}, and $C_{N\delta_i}$ terms was used. Third and fourth-order order Mach and α expansions were used for $C_{N\alpha}$ and C_{N_0} respectively. The final model used for all coefficients is given by:

$$
\begin{aligned}
C_a = {}& \beta_0 + \beta_1 \alpha + \beta_2 \alpha^2 + \beta_3 \alpha^3 + \beta_4 \alpha^4 + \beta_5 M_\infty + \beta_6 M_\infty^2 + \beta_7 M_\infty^3 \\
& + \beta_8 M_\infty^4 + \beta_9 M_\infty \alpha + \beta_{10} M_\infty \alpha^2 + \beta_{11} M_\infty \alpha^3 + \beta_{12} M_\infty^2 \alpha + \beta_{13} M_\infty^2 \alpha^2 + \beta_{14} M_\infty^2 \alpha^3 \\
& + \beta_{15} M_\infty^3 \alpha + \beta_{16} M_\infty^3 \alpha^2 + \beta_{17} q + \beta_{18} \dot{\alpha} + \beta_{19} M_\infty q + \beta_{20} M_\infty \dot{\alpha} + \beta_{21} \alpha q + \beta_{22} \alpha \dot{\alpha} \\
& + \beta_{23} \delta_{\text{OB}} + \beta_{24} \delta_{\text{IB}} + \beta_{25} M_\infty \delta_{\text{OB}} + \beta_{26} M_\infty \delta_{\text{IB}} + \beta_{27} \alpha \delta_{\text{OB}} + \beta_{28} \alpha \delta_{\text{IB}} \quad (3)
\end{aligned}
$$

where, in this work $a = N, m$.

This same model was used for all MULDICON planforms. In this form, the fit coefficients are solved by linear regression. All modeling is implemented using MATLAB.

4.4. Training Maneuver Generation

The training maneuvers used in this work are constructed from Schroeder signals [21]. Schroeder showed that harmonic, multi-sine signals could be optimized by peak factor to achieve a low-amplitude, mixed frequency signal. Morelli [22] extends the optimized Schroeder signal to N variables by combining every N^{th} harmonic frequency. Each resultant set of harmonic frequencies is separately optimized following Schroeder's process. These signals are orthogonal and have low correlation, which allows them to be applied to separate aircraft parameters and varied simultaneously. For this work, all Muldicon designs complete the same 40 second training maneuver. The
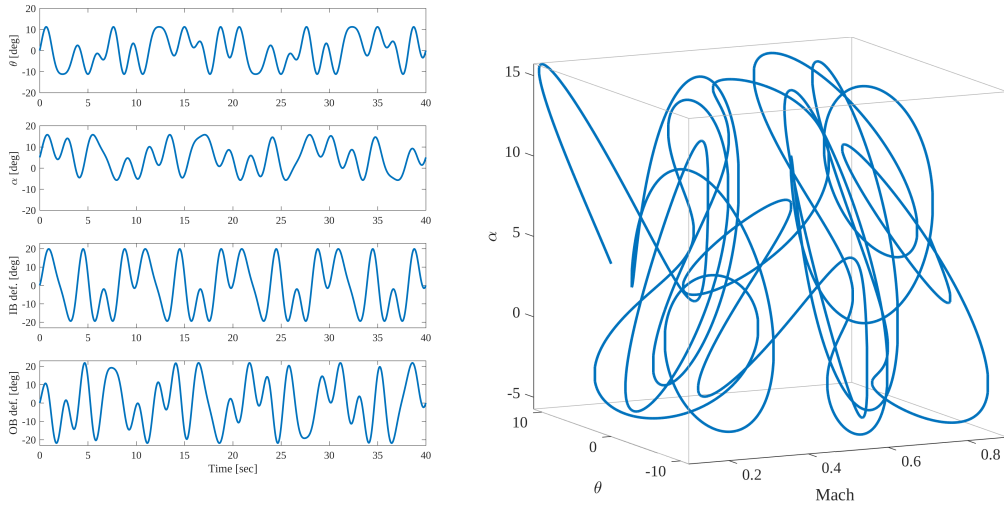

Figure 9: The Schroeder signals during the 40 second training maneuver (left), and the Mach-α-θ regressor coverage (right).

maneuver inputs are shown in Figure 9. Four Schroeder signals are generated to vary α, θ, IB, and OB deflection. Simultaneous to these inputs, the reference Mach condition is steadily changed from 0.1 to 0.9. This is executed by translating the mesh into the oncoming flow, increasing the relative Mach number of the aircraft. Morelli demonstrates the technique of changing reference condition 'behind' a training maneuver in Ref [23], with good success.

The Schroeder signals are generated using the SIDPAC [24] `mkmsswp.m` function. These signals are constructed from the harmonic frequencies ranging from the lowest frequency limited by

simulation length, up to $k = 0.075$. The angle of attack is set to vary by 20°, from-5 to 15°, and θ are set to vary around 0° by 20° as well. The control surface deflections are set to vary by 40°, between ±20°. This results in a maximum control surface deflection rate of 57.8° per second. The maximum pitch rate is 32.3° per second, and the maximum angle of attack rate was similar.

The training maneuver varies α independent of θ as this allows for the independent modeling of $\dot{\alpha}$ and q effects. This is achieved by varying α through 'plunging' maneuvers relative to the reference flow. The magnitude of the plunging changes as the reference Mach changes. Care is taken to ensure the magnitude of the velocity past the aircraft increased linearly and smoothly even with the additional translations needed to vary α and Mach.

5. Results and Discussion

5.1. Control Device Study

5.1.1. Spoiler

In the following section a study with a similar spoiler geometry like those applied to the DLR-F19 configuration have been assessed.

Similar to the experimental investigations the spoiler is also located on the upper and the lower side of the wingtip but is applied to the MULDICON. As in the wind tunnel test, the spoilers are deflected perpendicular to the flow with a deflection angle of $\delta_u = 90°$ on the upper and $\delta_l = 90°$ on the lower side. Within the study the influence of the positioning of the spoiler on the wingtip, specifically the relative distance of the spoiler between the LE and the TE was analyzed. Therefore the parameter x/c is defined as the relative distance between the LE and TE, where $x/c = 0$ is the position at the LE and $x/c = 1$ the position at the TE. Three different positions of the spoiler
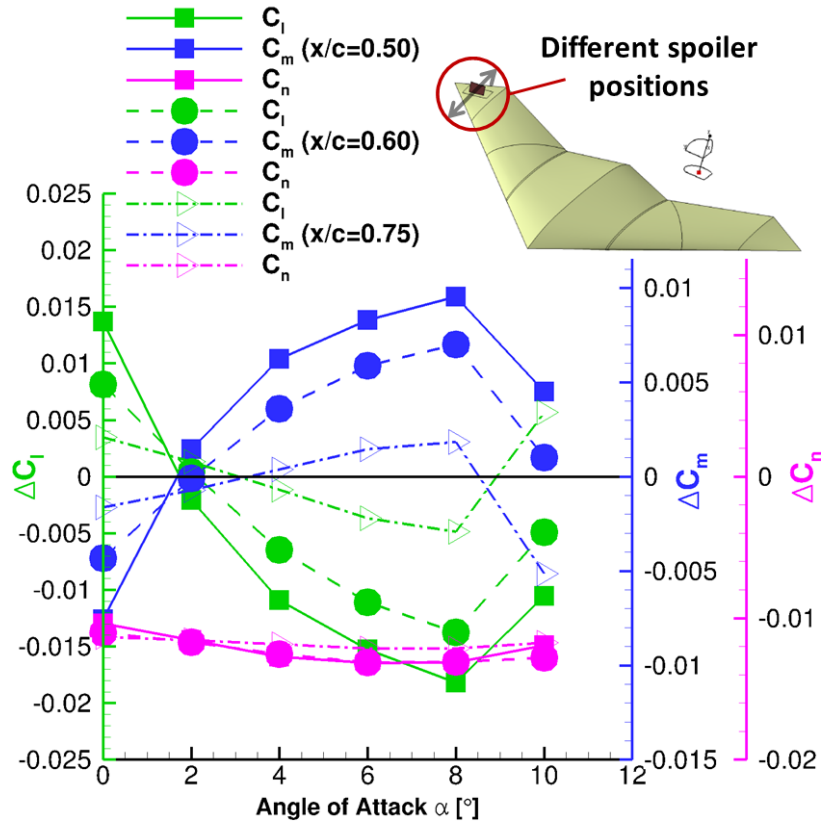

Figure 10: Moment distributions for different spoiler positions ($M_\infty = 0.4$, $Re_\infty = 55.9 \cdot 10^6$, $\delta_u = 90°$ and $\delta_l = 90°$).

were chosen. The relative distance of these positions are $x/c = 0.5$, $x/c = 0.6$ and $x/c = 0.75$. The deflection angle on both sides is the same for all positions. For all relative positions the

14

changes of the moment coefficients in comparison to the clean configuration are plotted versus the AoA in Figure 10. With increasing the relative position the gradients $\partial \Delta c_{l,m}/\partial \alpha$ decrease as well as the maxima of the rolling and pitching moment.

There are almost no changes in the yawing moment with changing the relative position. By changing the relative position from $x/c = 0.5$ to $x/c = 0.75$, the pitching moment is reduced by approximately 80% and the rolling moment by 75%. This means that the spoiler position should be as close as possible moved towards the TE to decrease the effect on the rolling and pitching moment sufficiently.

For a better understanding, the pressure coefficient through the spoiler along the chord for all spoiler positions are plotted in Figure 11.

Due to the spoiler, the lift on the wingtip is reduced in front of it. By increasing the relative distance x/c, the loss in lift is reduced. In the rear section of the spoiler, a zone with negative lift exists and by increasing the relative distance x/c, the negative lift is reduced due to the smaller rear section. Nevertheless, with the closest position of the spoiler to the TE a rear section with negative lift still exist. The total lift loss at the wing of the spoiler side causes a rolling moment. Reducing the lift loss means reducing the rolling moment.

Figure 11: C_P distribution through the spoiler along the chord ($M_\infty = 0.4$, $Re_\infty = 55.9 \cdot 10^6$, $\delta_u = 90°$ and $\delta_l = 90°$).

In addition, the negative lift in the rear section causes a pitch up effect which can be seen in Figure 10 represented by the positive change of the pitching moment. To minimize such pitch up effect, a configuration without a rear section is required. This tends to the configuration with a split flap where no rear section of the wing exists.

Before the control concept with the split flap is presented, the flow topology with the spoiler should be discussed. In Figure 10, it has been shown that a drop of the pitching moment from $\alpha = 8°$ to $\alpha = 10°$ is going along with an increase in rolling moment. The influences presented here are mainly applicable for attached flow conditions. However, at higher AoA, the flow topology changes. Figure 12 visualizes the change of the flow topology with spoiler between the AoA of $\alpha = 8°$ and $\alpha = 10°$. For $\alpha = 8°$ the tip vortex and the wake flow of the spoiler are separated. By increasing the AoA to $\alpha = 10°$ the tip vortex interacts with the spoiler and with the wake flow of the spoiler. This interaction will be called in the following as "control device vortex interaction".
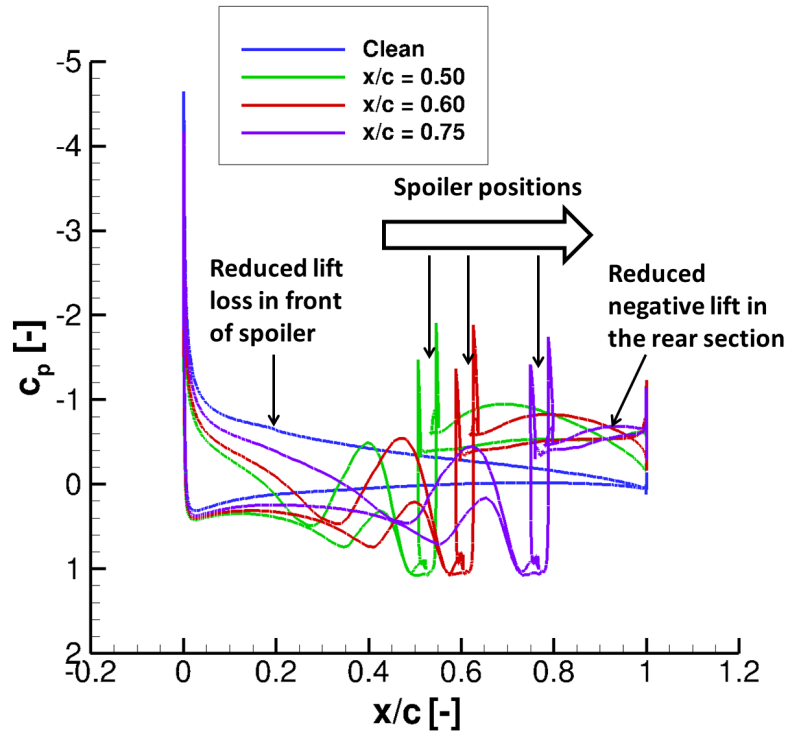
15
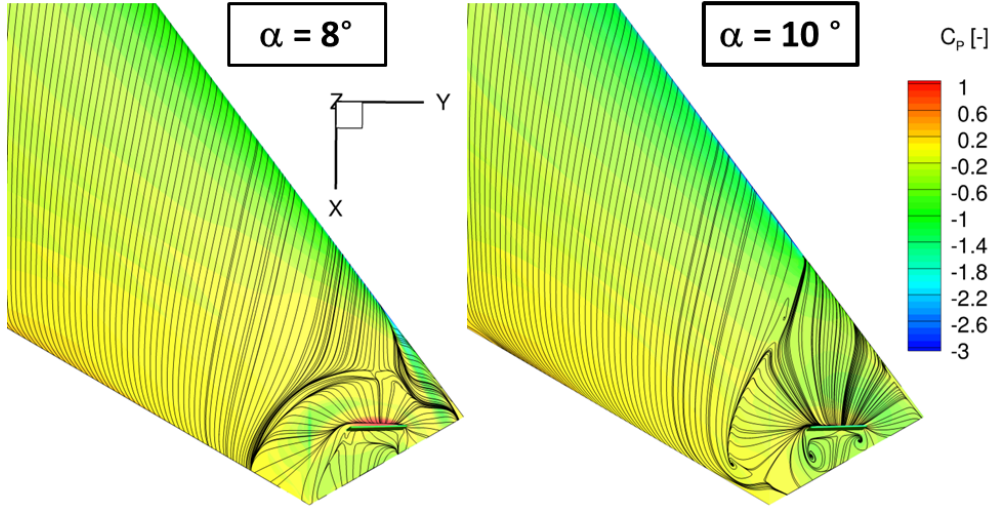
Figure 12: Comparison of the flow topology ($M_\infty = 0.4$, $Re_\infty = 55.9 \cdot 10^6$, $\delta_u = 90°$ and $\delta_l = 90°$).

In comparison to $\alpha = 8°$ the control device vortex interaction at $\alpha = 10°$ causes a change of the pressure distribution and a change of the moment coefficients. This causes the drop in pitching moment and an increase of the rolling moment as plotted in Figure 10. Looking at the experimental results of the DLR-F19 in section 3 the influence of the control device vortex interaction on the pitching moment coefficient can be observed as well, see Figure 6. Up to an AoA of $\alpha = 8°$ there are almost no variation in the pitching moment coefficient but for higher AoA the differences increase. Furthermore, the difference in the pitching moment of the full height spoiler is larger than the difference in the pitching moment of the 50% reduced height spoiler. The control device vortex interaction is an explanation for these differences in pitching moment at higher AoA as well as that the difference increase with a higher spoiler.

5.1.2. Split flap

Based on the conclusion regarding the spoiler investigations, a split flap might be a promising concept for effective yaw controllability. Therefore, a double sided split flap was designed for the wingtip. For the deflection of the split flap, a first estimation with empirical data was done. The deflection angles of $\delta_u = 45°$ for the upper split flap and $\delta_l = 32°$ for the lower split flap were kept constant. To analyze the effect of the vortical flow field on the control devices, CFD simulations with higher AoA and with different angle of sideslips (AoS) were performed with the TAU flow solver. The influence of the AoS on the yaw control device is quite crucial for the landing case. For the de-crab maneuver the yaw controllability must be guaranteed under crosswind condition. In Figure 13, the differences of the moment coefficients for the split flap in comparison to the clean configuration versus AoA for different AoS are plotted. First of all, a feasible yawing moment of $\Delta C_n \approx -0.016$ with ΔC_l and $\Delta C_m \approx 0$ could be achieved for attached flow conditions. These conditions apply up to an AoA of $\alpha = 10°$ and an AoS of $\beta = \pm 10°$. Therefore, the rolling, pitching and yawing moments are nearly constant versus AoA and AoS. For higher AoA like $\alpha = 10°$ the differences in rolling and pitching moment increase. In addition the yawing moment coefficient decreases. At an AoA of $\alpha = 14°$, the difference in rolling moment is three times higher and

16

the pitching moment is two times higher than the generated yawing moment. The decrease in the efficiency results from the tip vortex. As marked in Figure 13, the tip vortex occurs on the upper wing side at an AoA of $\alpha \approx 8°$ and is getting larger with increasing AoA. At the same time its onset point moves along the LE towards the apex. At an AoA of approx. $\alpha \approx 10°$, the tip vortex interacts with the control device and the interaction increases with higher AoA.
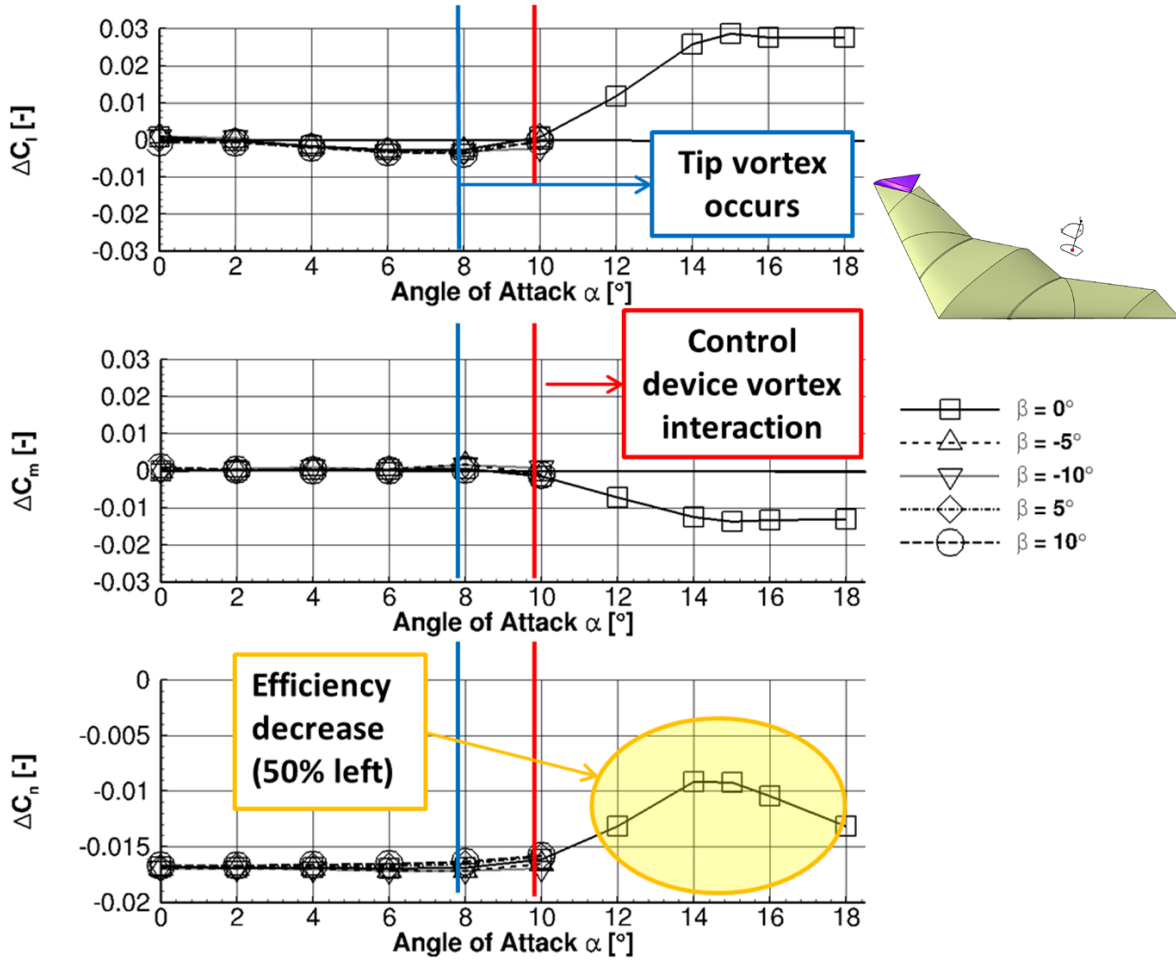

Figure 13: Moment distributions for the split flap with different angle of sideslips ($M_\infty = 0.4$, $Re_\infty = 55.9 \cdot 10^6$, $\delta_u = 45°$ and $\delta_l = 32°$).

In Figure 14, the control device vortex interaction is visualized. For $\alpha = 10°$, the tip vortex is interfering with the control device at the outer corner, so the upper split flap is slightly affected by the tip vortex. At a higher AoA of $\alpha = 15°$, the much larger tip vortex affects the entire split flap on the upper side of the wing.

Furthermore, the differences of the total pressure between the split flap side and the clean wing side in the wake flow decreases from the AoA of $\alpha = 10°$ to $\alpha = 15°$. This causes the decrease of the yawing moment.

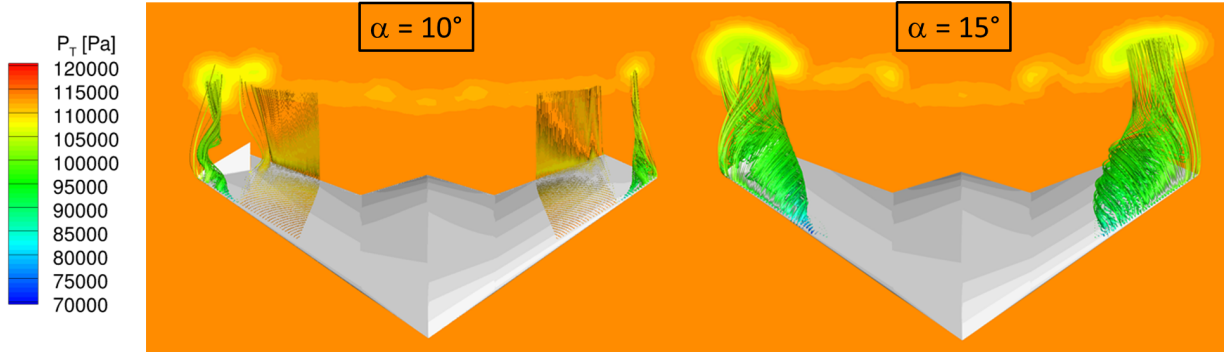Figure 14: Control device vortex interaction ($M_\infty = 0.4$, $Re_\infty = 55.9 \cdot 10^6$, $\delta_u = 45°$ and $\delta_l = 32°$).

5.2. System Identification

Static CFD runs are completed for Muldicon CCG and ASG wings designs. Four angles of attack were completed at $M_\infty = 0.4$ for designs 1 and 2, and at each condition, five control surface settings were simulated. Figure 15 compares the flow for both designs at $\alpha = 15°$, with no deflections, OB = $-20°$, and IB = $-20°$. This figure shows via streamlines one of the main differences between CCG and ASG wings, namely, a significant reduction in separated flow at the wingtip at high-α. The separated flow of ASG wing covers the outboard control surface significantly at this condition, reducing the control surface effectiveness. This behavior is most pronounced for negative control surface deflections. The other static results are shown with the SID modeling results, labeled in the figures as "Static CFD".

The 40 second Schroeder type training maneuvers for CCG and ASG wings were completed on the DoD HPCMP machines, Garnet and Excalibur. On Garnet for Muldicon CCG wing, the total simulation took 1.34 million CPU hours. The SID model fits for C_N and C_m during the training maneuver are shown in Figure 16. These show good matching to the training maneuver data, with normalized root mean squared error below 3.5%. The quasi-steady models do not capture the transient flow unsteadiness which is seen especially for C_m CFD data in Figure 16. However, another quasi-steady model can be fit to some measure of this unsteadiness to help quantify the variation in the aerodynamic coefficients models. No effort was made in this work to do this, however, Morton and McDaniel demonstrate the technique in [25]. Once constructed, the SID models are used to predict the aerodynamic behavior over the flight envelope tested by the static simulations. Comparisons between the static control surface deflections at varying α for C_N are shown in Figure 17, and C_m are shown in Figure 18. Figure 17 shows that the C_N behavior is quite linear for both designs for IB and OB control surface deflections up to $\pm 20°$. The SID models do a good job of predicting the coefficient values at these conditions, as well as control surface effectiveness which is apparent by the slope of the lines.

Figure 18 shows what was described in the static results section. Specifically, the loss of control surface effectiveness for negative deflections at high angles of attack. In this case, the SID models do capture the non-linearity of the control surface effectiveness for the ASG wing, and also predict some loss of effectiveness for the CCG wing for the OB deflection. Overall, the SID models match quite well with the static CFD results, with a few exceptions. Additionally, the trends of the control surface effectiveness are captured reasonably well by the models.
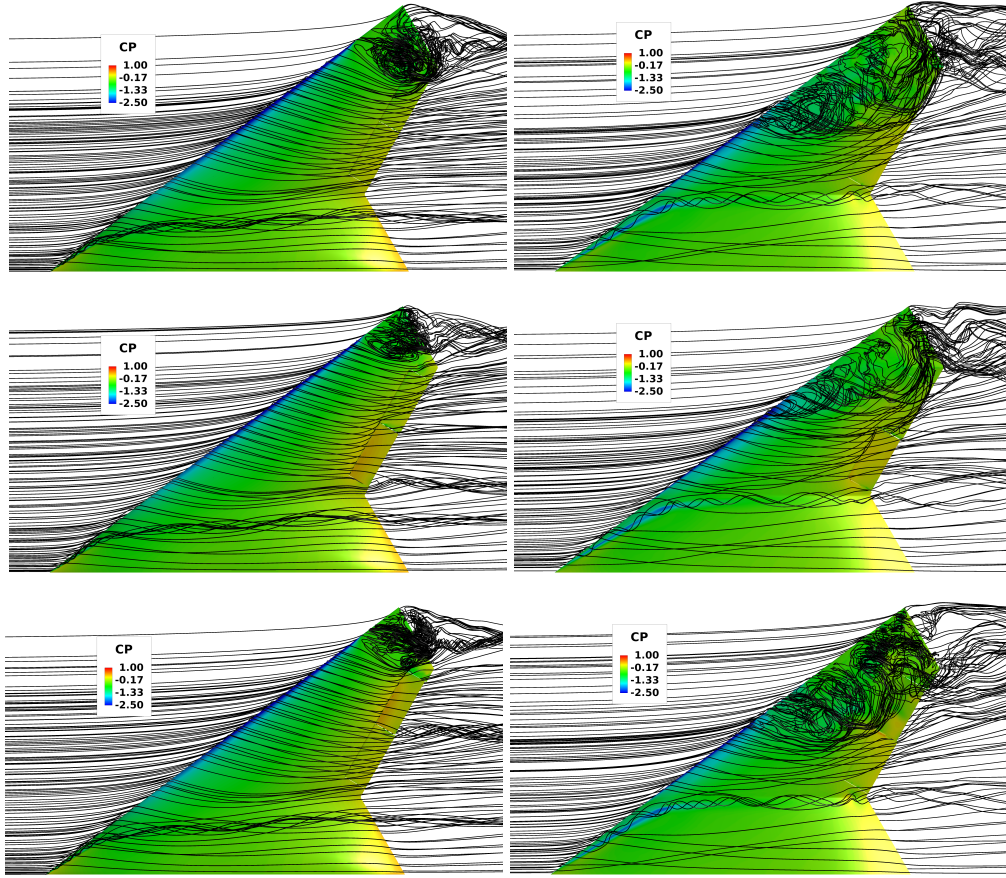
18

Figure 15: Muldicon CCG wing (left column) and ASG wing (right column) with no deflection (top row), IB = −20° (middle), and OB = −20° (bottom) (M_∞ = 0.4, Re_∞ = 55.9 · 10⁶).

The developed SID models are also used to simulate the integrated loads of a some off-design maneuvers. These maneuvers are doublet-type maneuvers with very fast transitions between dwell periods where none of the conditions change. The maneuvers excite transient dynamics that cannot be predicted by the quasi-steady models. However, the dwell portions of the doublets can be compared to the SID models to demonstrate the models' accuracy. Two separate doublet type maneuvers are completed. One is a simple pitch doublet, and one is an *IB* doublet followed by an *OB* doublet. Both maneuvers are completed at M_∞ = 0.5

Figure 19 shows the C_N response to two doublet maneuvers. Only C_N results are shown. The predictions of the steady state portions of the doublet maneuvers are quite close, with the SID models largely falling within a 10% band. The worst prediction of C_N is seen in the control surface doublet prediction for ASG wing.

ASG and CCG are two different designs with different aerodynamic performance. A strong feature of the CCG wing is vortical flow at high lift, particularly for low-speeds. The ASG of the NATO STO AVT-251 Task Group investigated a design approach to preserve attached flow over the MULDICON at high and low speeds. It has been shown that the ASG design with attached flow shows significant advantages in performance throughout the flight envelope compared with
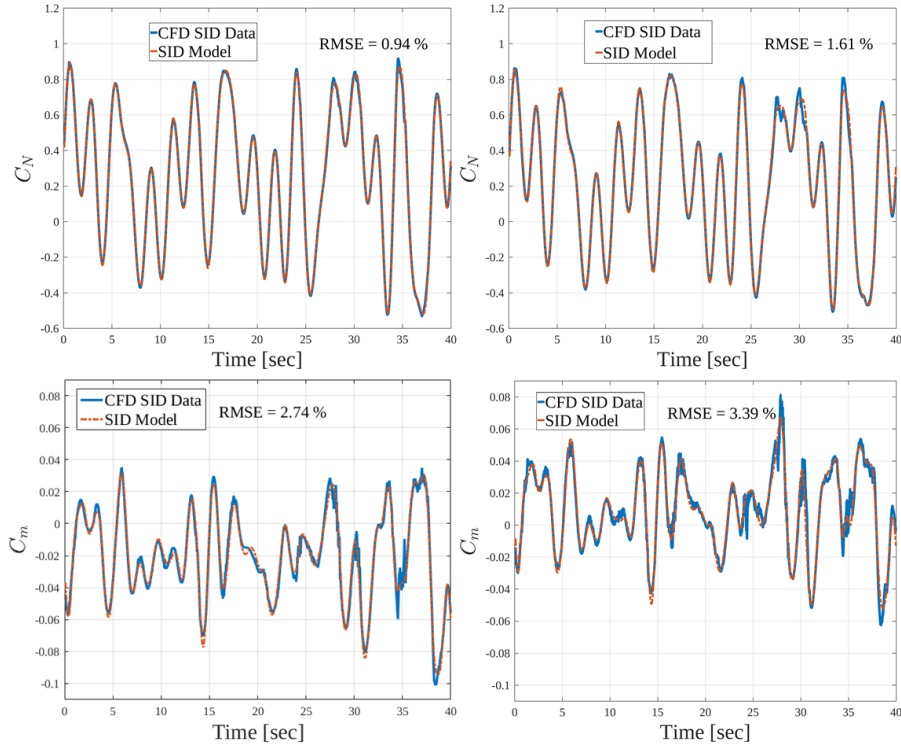
19

Figure 16: C_N (upper) and C_m (lower) model fits of the 40 second training maneuver, with Muldicon CCG wing (left column) and ASG wing (right column).
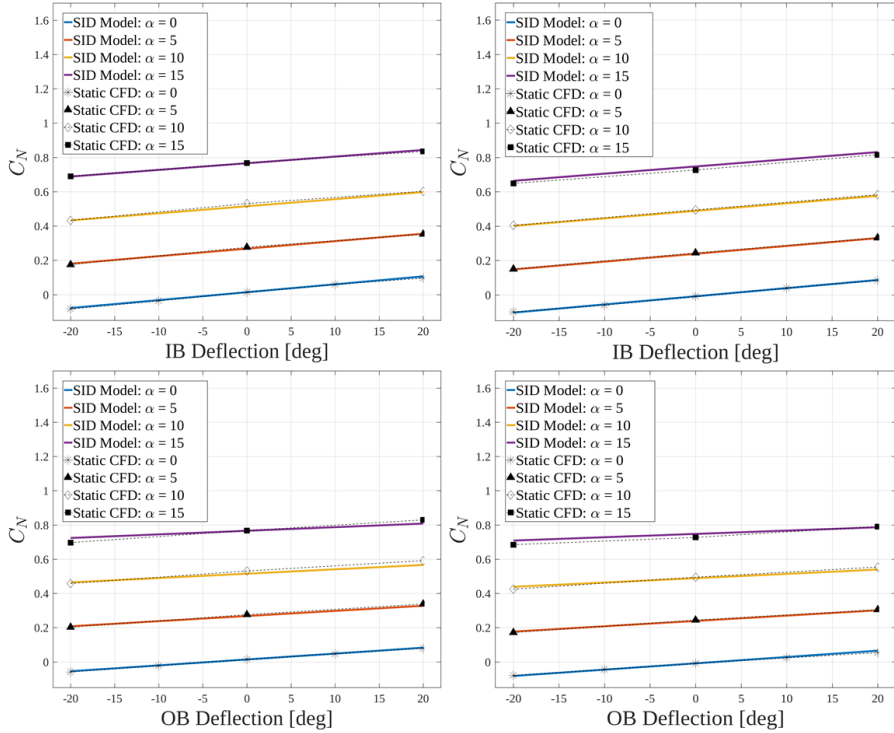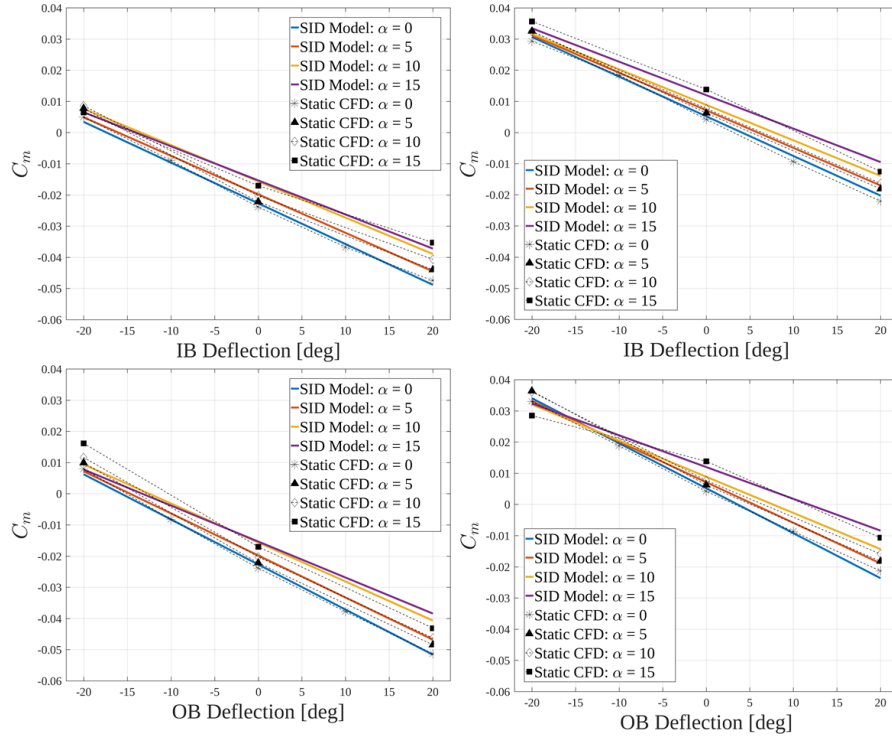

Figure 17: C_N vs. IB deflections (upper) and C_N vs. OB deflections (lower) comparing static CFD and SID model for Muldicon CCG wing (left column) and ASG wing (right column) at varying α ($M_\infty = 0.4$, $Re_\infty = 55.9 \cdot 10^6$).

Figure 18: C_m vs. IB deflections (upper) and C_m vs. OB deflections (lower) comparing static CFD and SID model for Muldicon CCG wing (left column) and ASG wing (right column) at varying α ($M_\infty = 0.4$, $Re_\infty = 55.9 \cdot 10^6$).
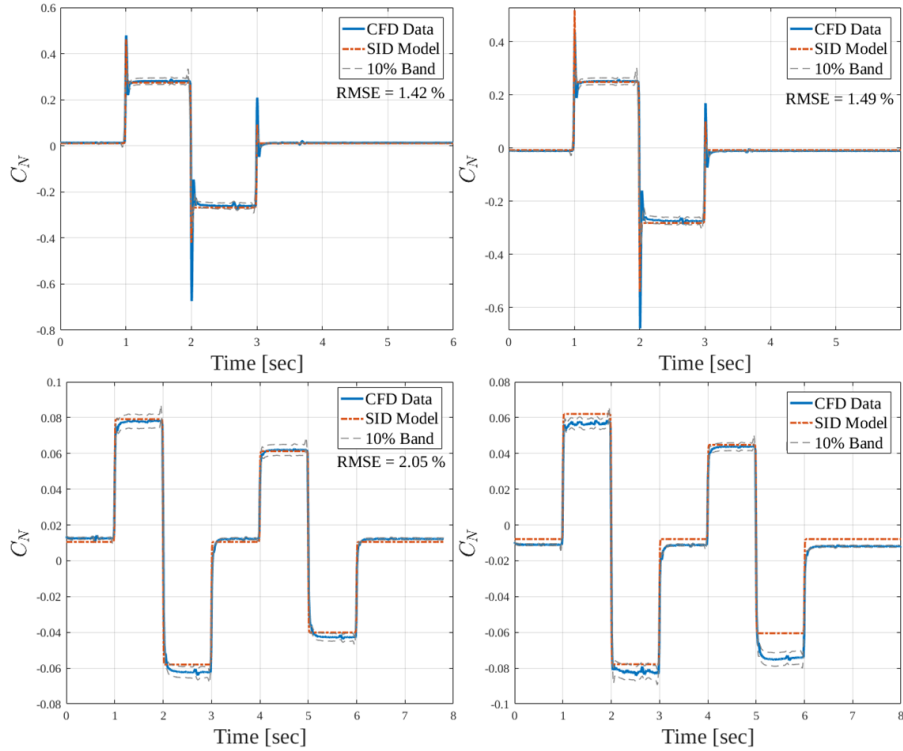

Figure 19: The pitch doublet (upper) and the control surface doublet (lower) comparing off-design CFD and SID model for CCG wing (left column) and ASG wing (right column) ($M_\infty = 0.5$, $Re_\infty = 55.9 \cdot 10^6$).

the CCG wing. See Figure 19, for example. CCG wing shows a drop in pitching moment increase with angle of attack from $\alpha = 10°$ to $15°$. The ASG still shows pitching moment increase at these angles. The SID still works nicely to capture the nonlinear behavior seen in the pitching moment of the CCG wing at high angles of attack.

In summary, the main reason to include both is to demonstrate the general capability of SID approach for difference configurations with different aerodynamic behavior.

6. Conclusions

In the present paper two different control concepts for yaw controllability are considered. The study is based on preliminary investigations carried out in experiments with spoilers applied to the DLR-F19 and numerical validations of different control devices applied to the MULDICON using the DLR RANS solver TAU. The experimental results show that a double sided spoiler positioned at the outer wing region generates an uncoupled yawing moment. The numerical results of the spoilers confirm that a position of the spoiler close to the trailing edge improves the behavior of such a control device. However, a control device vortex interaction occurs for higher AoA which decreases the efficiency of the upper spoiler and split flap respectively. The control device vortex interaction changes the aerodynamic topology and influences the moment coefficients. Spoilers and split flaps located close to the TE at the wingtip area are less sensitive regarding small AoA but the sensitivity increases for higher AoA.

Nevertheless a split flap is a feasible control device for yaw authority. For landing, AoA between $\alpha = 5°$ and $\alpha = 10°$ can be estimated with a Mach number smaller than the one considered here. The occurrence of the tip vortex depends on the flight condition as well as on the aerodynamic shape design. In the present study the control device vortex interaction occurs around an AoA of $\alpha = 10°$, which means that the range of AoA is covered by the split flap where no interaction occurs. For smaller Mach numbers the occurrence of the tip vortex is shifted to higher AoA. On the one hand to delay the interaction to higher AoA the design or the location of the split flap can be changed. On the other hand moving the split flap closer to the inner wing region decreases the efficiency because of the reduced lever arm and increases the influence of the split flap or spoiler on the rolling and pitching moments.

Additionally this work presents quasi-steady aerodynamic models that accurately and rapidly can generate aerodynamic data of a number of UCAVs. Schroeder-type forced motion were tested in this work. The motion covers the changes in angle of attack (α) from $-5°$ to $15°$, a Mach range from 0.2 to 0.8, and inboard and outboard control surface deflections between $\pm 20°$, while also independently modeling $\dot{\alpha}$ and pitch rate, q. The accuracy of the developed models were then compared to static data generated by CFD at test points across the flight-envelope, as well as against dynamic "off-design" maneuvers performed in CFD. Good agreement was found in most cases, while the cost of simulating the forced motion is much less than the cost of generating all aerodynamic data for all points in the input space. Indeed, this model here is demonstrated without the yaw control device, but it was shown that the model predicts the nonlinear effect due to the vortical flow accurately. Nevertheless a split flap at the outer wing region is more affected by the tip vortex as the *IB* or *OB* elevons, which means a higher nonlinear effect. For this reason the yaw control device will be included in the SID-Model in further investigation.

7. Acknowledgments

References

[1] R. M. Cummings, C. M. Liersch, and A. Schütte, "Multi-disciplinary design and performance assessment of effective, agile nato air vehicles," *AIAA Paper 2018–2842*, June 2018.

[2] R. K. Nangia, J. Coppin, and M. Ghoreyshi, "Ucav wing design, assessment and comparisons," *AIAA Paper 2018–2838*, June 2018.

[3] C. Liersch, K. Huber, A. Schütte, D. Zimper, and M. Siggel, "Multidisciplinary design and aerodynamic assessment of an agile and highly swept aircraft configuration," *CEAS Aeronautical Journal*, vol. 7, no. 4, pp. 677–694, 2016.

[4] M. Winkler and K. Huber, "Numerische bewertung innovativer steuerflächen einer generischen lamdaflügel-konfiguration," *EB*, vol. 124, p. 901, 2016.

[5] C. M. Liersch and G. Bishop, "Conceptual design of a 53deg swept flying wing ucav configuration," *AIAA Paper 2018–2839*, June 2018.

[6] M. Ghoreyshi, K. J. Badcock, and M. A. Woodgate, "Accelerating the numerical generation of aerodynamic models for flight simulation," *Journal of Aircraft*, vol. 46, no. 3, pp. 972–980, 2009.

[7] M. Ghoreyshi, A. J. Lofthouse, D. B. Findaly, and J. Lee, "Indicial methods for the numerical calculation of dynamic derivatives," vol. 55, no. 7, pp. 2278 – 2294, 2017.

[8] J. Allen and M. Ghoreyshi, "Forced motion design for aerodynamic identification and modeling of a generic missile configuration," *Aerospace Science and Technology*, vol. 77, pp. 742 – 754, 2018.

[9] R. Cummings and A. Schütte, "Assessment of stability and control prediction methods for nato air and sea vehicles," *AVT-161 Task Group, TR NATO RTO-TR-AVT-161*, April 2012.

[10] D. Zimper and D. Hummel, "Analysis of the transonic flow around a unmanned combat aerial vehicle configuration," *Journal of Aircraft*, vol. 55, no. 2, pp. 571–586, 2016.

[11] K. Huber, D. Vicroy, A. Schütte, and A. Hübner, "Ucav model design investigations and static low speed wind tunnel experiments to estimate control device effectiveness and s&c capabilities," *AIAA Paper 2014–2002*, June 2014.

[12] M. Galle, J. Evans, and T. Gerhold, *Technical Documentation of the DLR [Tau]-code*. DLR, Inst. für Strömungsmechanik, 1997.

[13] S. R. Allmaras and F. T. Johnson, "Modifications and clarifications for the implementation of the spalart-allmaras turbulence model," in *Seventh international conference on computational fluid dynamics (ICCFD7)*, pp. 1–11, 2012.

[14] Computational Research and Engineering Acquisition Tools And Environments (CREATE) - Air Vehicles, *HPCMP CREATEKestrel User's Guide, Version 7.0*. Sept 2016.

[15] CENTAUR, "Centaursoft, : http://www.centaursoft.com."

[16] C. M. Liersch and K. C. Huber, "Conceptual design and aerodynamic analyses of a generic ucav configuration," *AIAA Paper 2014–2001*, June 2014.

[17] A. Schütte, K. Huber, and D. Zimper, *Numerische aerodynamische Analyse und Bewertung einer agilen und hoch gepfeilten Flugzeugkonfiguration*. Deutsche Gesellschaft für Luft-und Raumfahrt-Lilienthal-Oberth eV, 2015.

[18] D. M. Nelson, J. P. Irving, M. Ghoreyshi, A. Jirásek, and A. J. Lofthouse, "Experimental and numerical investigation of flight dynamics of a generic lambda wing configuration," *Aerospace Science and Technology*, vol. 71, pp. 706–724, 2017.

[19] D. I. Greenwell, "Frequency effects on dynamic stability derivatives obtained from small-amplitude oscillatory testing," *Journal of Aircraft*, vol. 35, no. 5, pp. 776–783, 1998.

[20] V. Klein and E. A. Morelli, *Aircraft System Identification - Theory and Practice*. Reston, VA: American Institute of Aeronautics and Astronautics, 2006.

[21] M. R. Schroeder, "Synthesis of low-peak-factor signals and binary sequences with low autocorrelation," *IEEE Transactions on Information Theory*, January, 1970.

[22] E. A. Morelli, "Flight test maneuvers for efficient aerodynamic modeling," *American Institute of Aeronautics and Astronautics*, vol. 49, 2012.

[23] E. A. Morelli, "Efficient global aerodynamic modeling from flight data," *AIAA Paper 2012–1050*, January 2012.

[24] E. A. Morelli, "System IDentification Programs for AirCraft (SIDPAC)," *AIAA Paper 2002–4704*, August, 2002.

[25] S. A. Morton and D. R. McDaniel, "CFD-based model building of the F-16XL static and dynamic loads using Kestrel," *AIAA 2017-0286*, January 2017.